Alexandria Engineering Journal (2023) **66**, 873–889

HOSTED BY

ELSEVIER

Alexandria University

**Alexandria Engineering Journal**

www.elsevier.com/locate/aej
www.sciencedirect.com

# Aerodynamic characteristics of intercity train running on bridge under wind and rain environment

**Guang-Zhi Zeng** [a,b,c], **Zhi-Wei Li** [a,*], **Sha Huang** [a], **Zheng-Wei Chen** [b,c,‡]

[a] *School of Rail Transportation, Wuyi University, Jiangmen 529020, Guangdong Province, China*
[b] *National Rail Transit Electrification and Automation Engineering Technology Research Center (Hong Kong Branch), Hung Hom, Kowloon, Hong Kong, China*
[c] *Department of Civil and Environmental Engineering, The Hong Kong Polytechnic University, Hung Hom, Kowloon, Hong Kong, China*

Received 30 June 2022; revised 18 October 2022; accepted 22 October 2022
Available online 17 November 2022

**KEYWORDS**

Wind and rain environment;
Intercity train;
Bridge;
Aerodynamic characteristic

**Abstract** Severe weather, especially strong rain-loaded wind, appears in coastal areas frequently. The strong wind driving raindrops worsens the wind effect and aggravates its impact on the intercity railway bridge and running trains. Based on the Euler multiphase model, for evaluating the effect of raindrops in wind and rain environment on running trains, a numerical simulation approach was adopted in this study, and the influence of the crosswind speed and rainfall with varying characteristic parameters on the aerodynamic performances of intercity trains was analysed. The results showed that the airflow around the train drove some raindrops to show a parabolic projectile feature, and the projectile distance increased as the crosswind speed increased, but the projectile distance showed no noticeable change with the rise in the rainfall, because the impact of the crosswind played a dominant role, while the raindrops provided additional effects in the wind and rain environment. Furthermore, in the wind and rain environment, as the crosswind speed increased and compared to that of the 10 m/s conditions, an increase of 354.37 %, 369.60 % and 355.07 % in $C_S$, $C_L$ and $C_M$ of the whole train was shown in 30 m/s wind speed conditions, respectively, while, as the rainfall increased to 100 mm/h compared to that of the 20 mm/h, an increase of 6.41 % and 6.25 % in $C_S$ and $C_M$ of the whole train, as well as a decrease of 0.71 % in $C_L$ of the whole train was shown, respectively.

## 1. Introduction

Given the rising passenger volume of intercity commuters and demand for diverse transportation in metropolitan areas [1], intercity railways have rapidly developed in the urban agglomeration areas of China due to their high speeds, large volumes, safety, and reliability [2–8]. In recent years, bridges have

---

[*] Corresponding author.
E-mail addresses: lzhw1205@163.com (Z.-W. Li), zhengwei.chen@polyu.edu.hk (Z.-W. Chen).
[‡] Co-corresponding author.

Peer review under responsibility of Faculty of Engineering, Alexandria University.

https://doi.org/10.1016/j.aej.2022.10.058
1110-0168

played a dominant role in intercity railways owing to the integrative development of various modes of transportation between cities. However, compared to those running on the ground, the aerodynamic characteristics and safety of trains running on viaducts are more complicated, under the influence of environmental winds [9–15], which pose a significant threat to the operational safety and stability of intercity trains on bridges [16–21]. In addition, the coastal urban agglomeration in southeast China is located in the monsoon climate region. These areas are mainly affected by the wet warm airflow from the ocean in summer and are disturbed by strong convective weather, such as typhoons, accompanied by severe monsoon rainfall, which forms the combined effect of wind and rain. The strong wind driving raindrops in the wind and rain environment worsens the turbulent effect of pulsating wind, which aggravates its impact on intercity trains running on bridges. Large areas and continuous strong wind and rain will have significant impacts on the regular operation of trains, such as causing train malfunctions, delays, and even overturning accidents [22]. In light of this, the aerodynamic characteristics associate with trains on bridges under the combination of wind and rain therefore require an in-depth analysis.

The impact effect of raindrops driven by wind on structure surfaces has attracted extensive attention in engineering fields such as buildings [23,24] and bridges [25], and the transportation field [26–29]. However, in terms of the high-speed trains, performing a full-scale experiment and wind tunnel test for investigating the aerodynamic performances in wind and rain environments is a tough challenge, owing to cost and technology factors. Therefore, researchers have mainly used numerical simulations to carry out research, for example, Shao et al. [26] adopted an Euler multiphase model to analyse the aerodynamic characteristic and operational stability of trains on the ground under heavy rain. In addition, Yue et al. [30] indicated that, under the force of rain-load wind, the operational stability of trains tends to reduce when a train runs on the ground, due to its aerodynamic loads increased. Furthermore, some researchers used a coupled Eulerian–Lagrangian method to simulate wind and rain environments. Jing and Gao [31] proposed a combined method using a turbulent model and a discrete phase model to analyse the raindrop density distribution around the carriage of a train with different crosswind speeds and amounts of rainfall. Du and Ni [32] further revealed the influence of raindrop particles on the airflow around the train base on the lower atmospheric boundary layer wind field using the Marshall–Palmer raindrop spectrum model. Yu et al. [33] analysed the airflow characteristics around a train on the ground and the relation between the aerodynamic load coefficient and rainfall at different operating speeds.

As mentioned above, trains running on the ground have been the subject of previous studies focusing mainly on their aerodynamic performances. Different from earlier studies, based on the three-dimensional numerical simulation method and Euler multiphase model, an intercity train operating on a bridge under rain and wind environments in terms of its comprehensive aerodynamic performances were taken into account in this work, and the influences of different parameters of the wind and rain environment were also considered in detail.

Section 2 describes the numerical details, including the parameter settings of the wind and rain, computational model, domain, mesh generation, and solve settings. Section 3 describes the validation of the numerical method. Then, a detailed result analysis and discussion are presented in Section 4. Finally, the main conclusions are drawn in Section 5.

## 2. Numerical method

### 2.1. Governing equations

Due to the large number and discontinuous feature of raindrop particles in a numerical simulation of the wind and rain environments, turbulent transport around the train affects its aerodynamic performance significantly. As the Euler multiphase model can comprehensively explore in great detail of raindrops' turbulent action on the aerodynamic characteristics of complex objects [26], in the current work, an Euler multiphase model was used to carry out the numerical simulation of the wind and rain coupled environment. The Euler multiphase model distinguishes different independent phases based on the physical properties and dynamic responses of the materials, so both air and raindrops with different diameters were regarded as a continuous medium, and the volume fraction was introduced to represent the volume ratio of each phase in the flow field to solve the governing equations [34].

#### 2.1.1. Wind phase

Most of the flow phenomena associated with trains are turbulent flow phenomena, so a turbulence model was adopted in this paper. Due to higher computational requirements and time costs, the large eddy simulation (LES) and detached eddy simulation (DES) are hard to using for engineering application research, even if they can capture more detailed flow structures. Nevertheless, for resolving engineering turbulence in train aerodynamics, the Reynolds-averaged Navier–Stokes (RANS) method based on the standard $k$-$\varepsilon$ turbulence model is also suitable for simulating the flow field around a train in crosswind conditions using similar geometries, owing to its better computational cost, stability, and accuracy [35–37]. Furthermore, for the wind phase, using the standard $k$-$\varepsilon$ model can achieve good consistency with experimental results in the study of building structures under wind and rain environments [38,39]. Therefore, the steady standard $k$-$\varepsilon$ turbulent model was adopted herein, and the governing equations for the wind phase in the present work based on the steady standard $k$-$\varepsilon$ model were described by the following equations [38]:

$$\frac{\partial u_j}{\partial x_j} = 0 \tag{1}$$

$$\frac{\partial(\rho_a u_i u_j)}{\partial x_j} = -\frac{\partial p}{\partial x_i} + \frac{\partial \tau_{ij}}{\partial x_j} \tag{2}$$

$$\frac{\partial(\rho_a k u_j)}{\partial x_j} = \frac{\partial}{\partial x_i}\left[\left(\mu + \frac{\mu_t}{\sigma_k}\right)\frac{\partial k}{\partial x_j}\right] + G_k - \rho_a \varepsilon \tag{3}$$

$$\frac{\partial(\rho_a \varepsilon u_j)}{\partial x_j} = \frac{\partial}{\partial x_j}\left[\left(\mu + \frac{\mu_t}{\sigma_\varepsilon}\right)\frac{\partial \varepsilon}{\partial x_j}\right] + C_{1\varepsilon}\frac{\varepsilon}{k}G_k - C_{2\varepsilon}\rho_a\frac{\varepsilon^2}{k} \tag{4}$$

$$\mu_t = C_\mu \rho_a \frac{k^2}{\varepsilon} \tag{5}$$

where $\rho_a$ denotes the density of air, $p$ represents the pressure, $\tau_{ij}$ is the Reynolds stresses, $G_k$ is the generation of turbulence kinetic energy, $\sigma_k$ and $\sigma_\varepsilon$ represent the turbulent Prandtl number corresponding to the turbulence kinetic energy $k$ and the turbulence dissipation rate $\varepsilon$, respectively, $\mu$ represents the dynamic viscosity of air, and $\mu_t$ represents the dynamic turbulent viscosity of air. For the standard $k$-$\varepsilon$ model, the following model constants were specified, which were widely used in relevant research of wind and rain environment simulations previously[38–41]: $C_{1\varepsilon} = 1.44$, $C_{2\varepsilon} = 1.92$, $C_\mu = 0.09$, $\sigma_k = 1.0$, and $\sigma_\varepsilon = 1.3$.

### 2.1.2. Rain phase

In order to describe the multiphase flow by a continuous phase with mutual permeability, the volume fraction was introduced. According to this term, each phase occupied a different volume in the flow field. For additional phase representing the rainfall, the multiphase governing equations of the mass and momentum conservation can be written as follow [39]:

$$\frac{\partial\left(\rho_w \alpha_k u_{k,j}\right)}{\delta x_j} = 0 \tag{6}$$

$$\frac{\partial\left(\rho_w \alpha_k u_{k,i} u_{k,j}\right)}{\partial x_j} = \rho_w \alpha_k g + \rho_w \alpha_k \frac{3\mu}{\rho_w D^2} \frac{C_D Re_p}{4} \left(u_i - u_{k,i}\right) \tag{7}$$

where $\alpha_k$ is the volume fraction of $k$th rain phase, $u_{k,i}$ and $u_{k,j}$ denote the velocity components of $k$th rain phase along the $i$ and $j$ directions, respectively, $u_i$ is the wind velocity component in the $i$ direction, $\rho_w$ denotes the raindrop density, $g$ represents the gravitational acceleration, and $C_D$ and $\mathrm{Re}_p$ represent the raindrop drag coefficient and the relative Reynolds number, respectively.

## 2.2. Parameters of wind and rain environment

### 2.2.1. Initial condition of wind field

To accurately assess the wind and rain effect on a train on a bridge, the initial condition of the crosswind was determined by the lower atmospheric boundary layer wind field. For the average wind speed profile of horizontal uniform terrain, the regularity of exponential distribution in height can be described as follows [42]:

$$\frac{v_{wind}}{v_{windr}} = \left(\frac{h}{h_0}\right)^{\alpha} \tag{8}$$

where $v_{wind}$ is the average crosswind speed at the height of $h$, $v_{windr}$ donates the average crosswind speed at the standard reference height, $h$ represents the height, and $h_0$ and $\alpha$ are the standard reference height and ground roughness index, respectively. According to previous studies of the railway terrain [43–46], in open terrain, $h_0 = 10$ m and $\alpha = 0.16$. The crosswind speed range of 10–30 m/s and interval of 5 m/s were considered in the present study.

### 2.2.2. Raindrop size distribution

The proportions of raindrops with different diameters in the rainfall are the called raindrop size distribution, which makes it possible to be determined into different groups depending on the raindrop size spectrum, based on the modified $\Lambda$ distribution function [47].

$$N(D,R) = N_0 D^{\beta} e^{-\Lambda D} \tag{9}$$

where $D$ represents the raindrop diameter, $\beta$ donates an exponential constant equal to 2.93, and $N_0$ and $\Lambda$ are functions of the rainfall amount $R$. $N_0$ and $\Lambda$ are described as follows, based on the standard atmospheric pressure:

$$N_0(R) = 1.98 \times 10^{-5} R^{0.186} \left[1.047 - 0.0436\ln(R) + 0.00734(\ln(R))^2\right] \tag{10}$$

$$\Lambda(R) = 5.38 \times R^{0.186} \tag{11}$$

### 2.2.3. Terminal velocities of raindrops

When the gravity and aerodynamic forces are combined, the velocity of a raindrop increases gradually with the increase in the falling distance until it reaches an equilibrium state and falls at a constant speed. The terminal velocity of raindrops can be expressed as follows, based on the Atlas model [48]:

$$V_t(D) = \begin{cases} 0; & D \leqslant 0.03 \quad mm \\ 4.323(D - 0.03); & 0.03 \quad mm < D \leqslant 0.6 \quad mm \\ 9.65 - 10.3e^{-0.6D}; & D > 0.6 \quad mm \end{cases} \tag{12}$$

where $V_t\,(D)$ is the terminal velocity of the raindrop.

### 2.2.4. Drag coefficient

The motion of raindrops in the flow field is mainly determined by the gravitational and drag forces [49]. Under the wind and rain conditions, due to the flow field around a train presents the high-Reynolds-number characteristics of under the action of strong crosswinds, the Morsi–Alexander model was introduced to describe the drag forces on the raindrops. The equation of motion of a single raindrop can be expressed as follows [34]:

$$m_p \frac{d\overrightarrow{v_p}}{dt} = C_D \times \frac{1}{2}\rho_q \left(\overrightarrow{v_p} - \overrightarrow{v_q}\right)^2 A_p \tag{13}$$

where phases $p$ and $q$ donate the rain phase and wind phase, respectively, $A_p$ represents the surface area of a spherical raindrop, $m_p$ donates the mass of a single spherical raindrop, $\rho_q$ donates the physical density of phase $q$, $\overrightarrow{v_p}$ and $\overrightarrow{v_q}$ are the velocities of phases $p$ and $q$ in the space coordinate, respectively, and $C_D$ and $\mathrm{Re}_p$ are the drag coefficient and relative Reynolds number, respectively, which can be expressed as follows [34]:

$$C_D = a_1 + \frac{a_2}{Re} + \frac{a_3}{Re^2} \tag{14}$$

$$Re_p = \frac{\rho\left|\overrightarrow{v_p} - \overrightarrow{v_q}\right| D}{\mu} \tag{15}$$

where, $a_1$, $a_2$, and $a_3$ are constant, which is referenced by ANSYS [34].

### 2.2.5. Volume fraction of rain phase

Based on the terminal velocity, rainfall, and raindrop size distribution, the volume fraction $a_k$ of the rain phase with raindrop size $D$ can be expressed as follows [50]:

$$a_k = \frac{R f_h(D,R)}{V_t(D)} \frac{1 \times 10^{-3}}{3600} \tag{16}$$

where $f_h(D,R)$ denotes the fraction of the rain flux corresponding to raindrops with diameter $D$, which is given by [50]:

$$f_h(D,R) = \frac{D^3 N(D,R) V_t(D)}{\int_0^\infty D^3 N(D,R) V_t(D) dD} \tag{17}$$

The terminal velocities and volume fractions of raindrop particles with different raindrop diameters are shown in Figs. 1 and 2, respectively, which shows that the volume fraction of raindrops smaller than 1.50 mm was significantly higher than that of the others. Due to the relative concentration of the raindrop distribution, the raindrop particle diameters with higher volume fractions can be grouped to represent the raindrop distribution with similar sizes in the flow field space. Based on the above analysis, raindrops with diameters of 0.25–1.50 mm were selected for numerical calculations, and the particle size grouping interval was 0.25 mm. A rainfall range of 0–100 mm/h with an interval of 20 mm/h was considered in this paper.

### 2.3. Computational model

An intercity train comprising three cars was investigated in this work. As shown in Fig. 3, the lengths of the head and tail cars were both 25.45 m, and that of the middle car was 24.50 m. The total length, width, and height were $L$ = 76.30, $W$ = 3.33, and $H$ = 3.86 m, respectively. As shown in Fig. 4, the total width and height of the bridge were 12.2 and 3.5 m, respectively, and it was 15.0 m above the ground.

### 2.4. Computational domain and boundary conditions

Fig. 5 shows that the total length, width, and height of the computational domain were 53$H$, 72$H$, and 20$H$, respectively, where $H$ is the height of the train. The distance between the nose of the streamlined head car and the face ABCD and the transverse distance between the centre line of the train and the face BFGC were both 24$H$.

In terms of boundary conditions setting, the faces ABCD and BFCG were both set as a velocity-inlet, and the incoming flow was initiated with the velocity component in the velocity-inlet boundary conditions, as shown in Fig. 6. The faces EFGH and AEHD contrasted to the velocity-inlet were set as zero-pressure-outlet boundary conditions. In order to ensure that the results could be compared, the top surface DCGH was also set as a velocity-inlet, with a value of zero. Because it was far from the geometric model, the boundary condition setting of the top face would not affect the flow field around the train and bridge. Besides, for a realistic simulation of relative motion, all of the surfaces on the ground and the bridge were configured as moving no-slip walls and same with the train speed. Also, the stationary wall boundary conditions were configured to both train and bogie surfaces.

In the wind and rain environment, the boundary conditions were the same as in the crosswind simulation. For the rain phase, considering the effect of rain driven by crosswinds, the raindrops were released from the top face DCGH, front face ABCD, and side face BFGC. Furthermore, there are assumed no relative motions between the rain phase and wind phase in the horizontal direction, which means that the velocities of the raindrops were determined to be the same as the velocities of incoming flow in the horizontal direction, and the vertical velocities of the raindrops were determined by formula (12). The initial volume fraction of raindrops at the inlet of the computational domain was determined by formula (16).

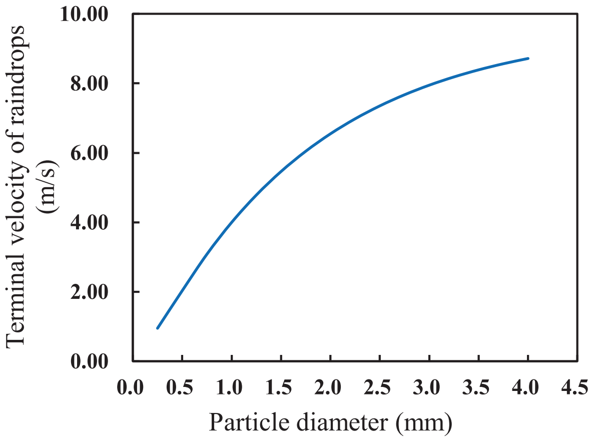

**Fig. 1** Variation of raindrop terminal velocity with particle diameter.

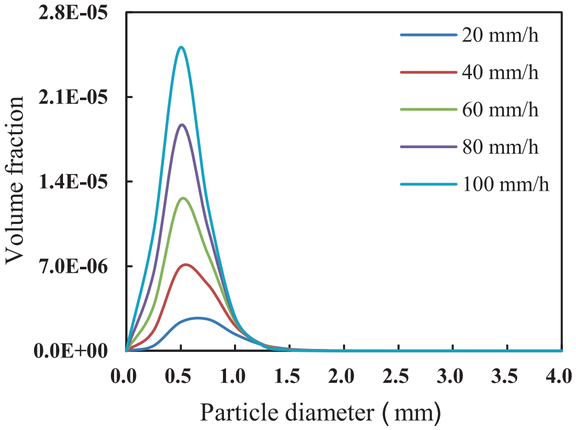

**Fig. 2** Variation of raindrop volume fraction with particle size for different rainfall amounts.

### 2.5. Grid generation

The domain was discretised based on an unstructured trimmer grid in Star-CCM+. The grid was finer around the complex structures of the train, such as the bogie and the region around the train cars, to capture details of occurring flows close to the structures. Considering to avoid the mesh sensitivity, a coarse mesh consisting of 10 million cells, a medium mesh consisting of 25 million cells, and a fine mesh consisting of 40 million cells were established, and the coefficients of the side force $C_S$, lift force $C_L$, and rolling moment around the leeward side rail $C_M$ of each carriage of the train were compared. These are defined as follows:

$$C_S = F_S / \left(0.5 \rho A V_{couple}^2\right) \tag{18}$$

$$C_L = F_L / \left(0.5 \rho A V_{couple}^2\right) \tag{19}$$

$$C_M = M_T / \left(0.5 \rho A l V_{couple}^2\right) \tag{20}$$

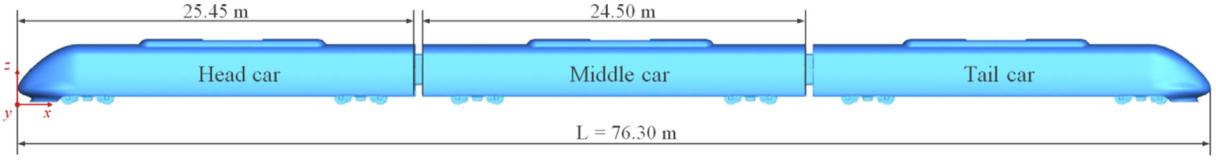

**Fig. 3** Intercity train model.

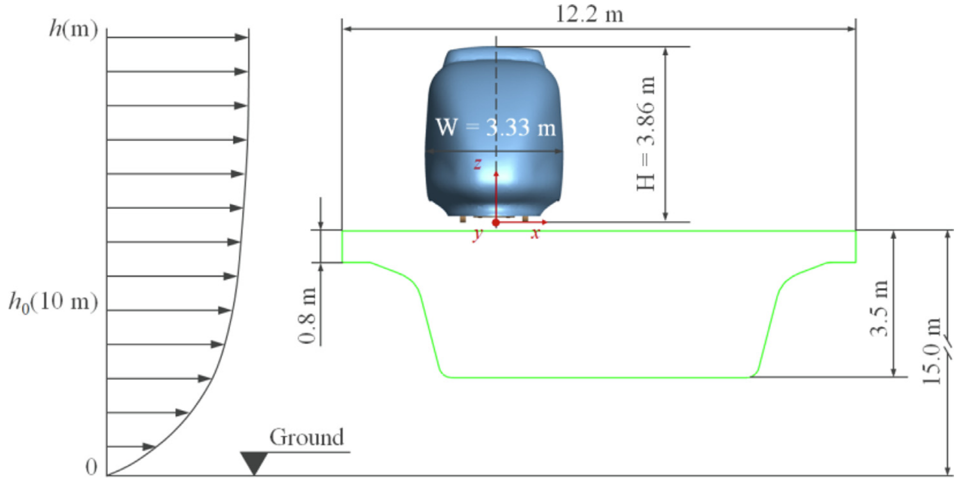

**Fig. 4** Intercity train and bridge.

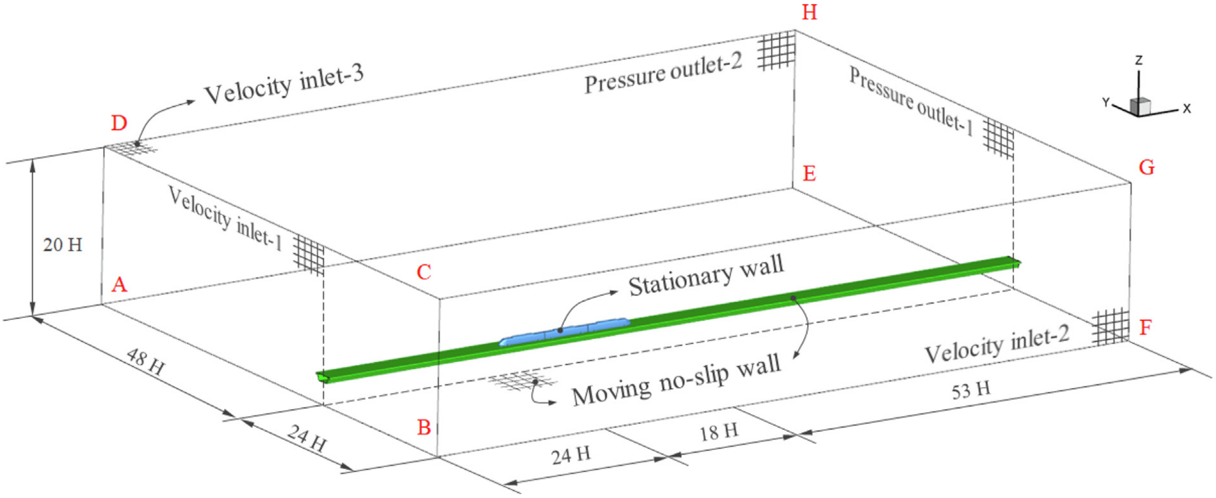

**Fig. 5** Computational domain.

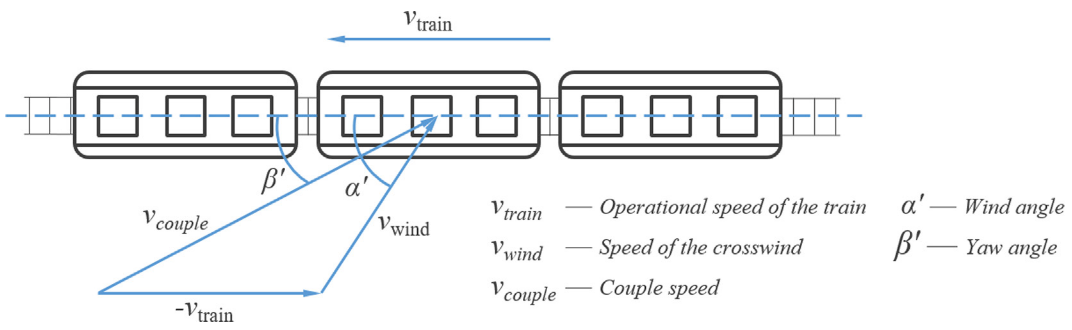

**Fig. 6** Definition of coupled wind speed parameters.

where $F_S$, $F_L$, and $M_T$ are the side force, lift force, and rolling moment around the leeward side rail of the train, respectively; $A$ and $l$ represent the reference area with 11.22 $m^2$ and the reference length with 3 m for the full-scale size, respectively [51]; $\rho$ is the air density; $v_{couple}$ is a coupled speed based on the train's running speed and the crosswind speed, which is defined in Fig. 6.

The aerodynamic load results of the head car from all three meshes are shown in Table 1. The deviations $\eta$ of the aerodynamic load coefficient between the coarse and medium meshes were about 5 %, but about 1 % between the medium and fine meshes, which indicated that it could meet the need of engineering applications. Considering the calculation accuracy and computational time cost comprehensively, the medium mesh was adequate. Fig. 7(a) and (b) show the grid on the train, bridge, and bogie surface, and Fig. 7(c) shows the mesh of the top view of the refinement region. The $y^+$ distribution on the train surface for the different meshes was in the range of 30–150, meeting the requirement of the standard $k$-$\varepsilon$ turbulence model.

### 2.6. Solver settings

The flow field was simulated based on the Euler multiphase model and steady standard $k$-$\varepsilon$ turbulence model [39]. Given that the 200 km/h train speed was thought to be the highest operating speed on China's intercity line, according to Anderson [52], the flow could be reasonably assumed to be incompressible, owing to the corresponding Mach number $Ma < 0.3$. Therefore, a pressure-based incompressible solver was adopted in the current work, and the Phase Coupled Semi-Implicit Method for Pressure Linked Equations (SIMPLE) algorithm was employed to solve the pressure and velocity coupling equations [26]. The gradients in the control volumes were calculated using the Green-Gauss cell-based method, while convection and diffusion terms were resolved by the second-order upwind scheme [48].

## 3. Result validation

In Section 2.5, the grid generation and mesh independence were discussed. Due to the high requirements of the train's full-scale test and wind tunnel experiment in the wind and rain environment, there is still no laboratory providing the test conditions and publishing relevant testing data. To verify the reliability of the numerical simulation presented in this paper, two existing wind tunnel data were employed for validation, including a train under crosswinds conducted by Zhang et al. [12], as shown in Fig. 8, while an airfoil suffering wind and rain coupled action measured by Bezos et al. [53], as shown in Fig. 9. Furthermore, the numerical method, mesh strategy, and other relative settings of the simulations related to the wind tunnel tests were the same as described above.

**Table 1** Computational grid and mesh independence verification.

| Mesh | $C_S$ | $\eta_S$ | $C_L$ | $\eta_L$ | $C_M$ | $\eta_M$ |
|---|---|---|---|---|---|---|
| Coarse | 0.8264 | / | 0.1349 | / | −4.6579 | / |
| Medium | 0.8063 | −2.43 % | 0.1278 | −5.23 % | −4.5546 | −2.22 % |
| Fine | 0.7987 | −0.95 % | 0.1264 | −1.11 % | −4.5157 | −0.85 % |

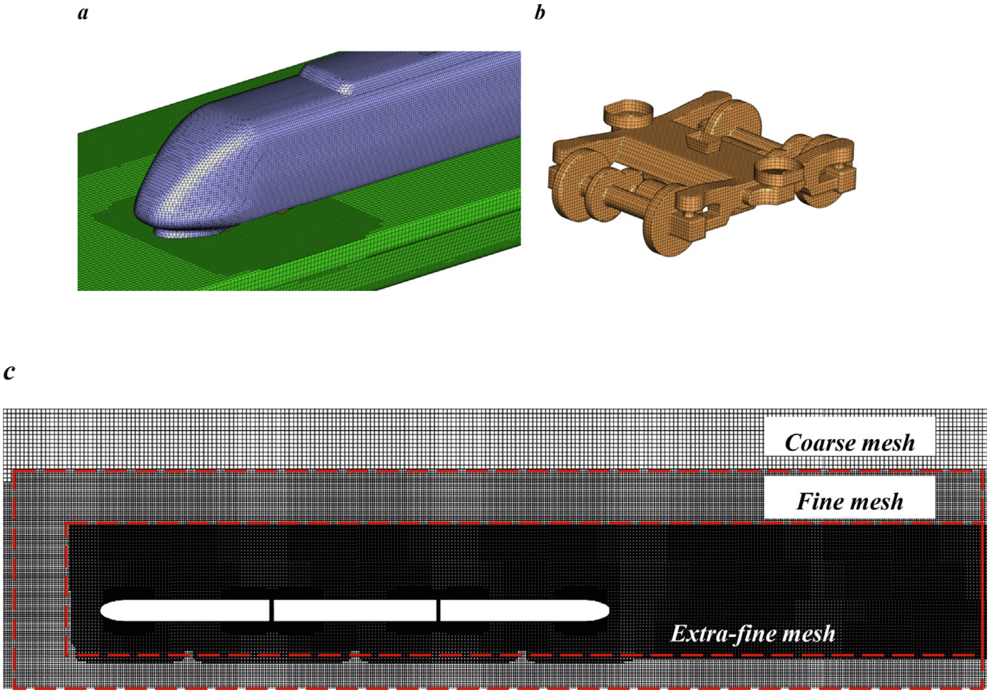

**Fig. 7** Computational grid: (a) grid on train and bridge surface, (b) grid on bogie surface, and (c) grid for the computational domain.

### *3.1. Wind tunnel test of the train under crosswind*

A wind tunnel test for a 1:8 scaled high-speed train under crosswinds reported previously was used for validation [16,17]. As shown in Fig. 8, there was one rotated slab with a 7 m diameter that can rotate 0° to 360° for varying yaw angles, while other parts are fixed. Besides, approximately 1.06 m of height separated the top of the slab from the ground of the wind tunnel to reduce the effects of the boundary layer. The aerodynamic forces of the train were investigated in an 8 m × 6 m large-scale low-speed wind tunnel at the China Aerodynamic Research and Development Centre based on six-component balances [12]. The simulation was performed using wind speed which was the same as the wind tunnel test at a yaw angle of 19.8°, with a corresponding Reynolds number of $1.89 \times 10^6$ based on the height of the train model and kinematic viscosity of $1.47 \times 10^{-5}$ $m^2/s$.

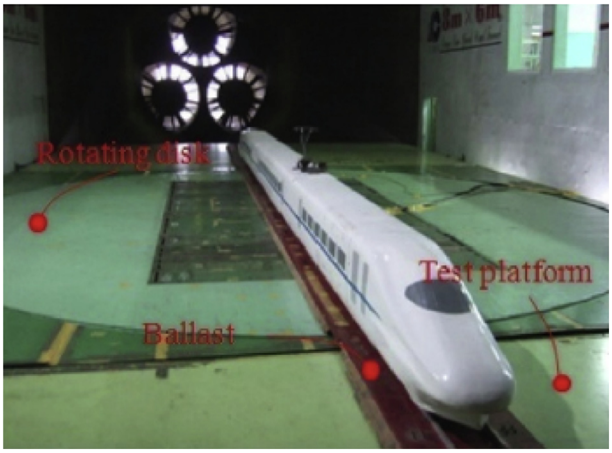

**Fig. 8** Wind tunnel and train model (adapted from Zhang et al. [12]).

The discrepancy of the aerodynamic forces between the wind tunnel test and the simulation, as shown in Fig. 10, indicated that the numerical method used in the present work was feasible for further CFD analysis, owing to the differences less than 5 %. Furthermore, the train's aerodynamic forces were predominated by the flow structures, so it could also be indirectly proven that the analysis of the flow structures in this paper was acceptable, and this indirect approach was also used in previous studies [54].

### *3.2. Wind tunnel test of the airfoil under wind and rain*

For the coupled flow field of the wind and rain, the aerodynamic performance result of the NACA 64–210 aerofoil measured by Bezos et al. [53] in the NASA wind tunnel under the strong rain conditions, as shown in Fig. 9, was used to verify the accuracy of the numerical method in this paper. The subsonic wind tunnel had a height of 14 ft (4.27 m) and a width of 22 ft (6.71 m). The aerofoil model had a chord length of 2.5 ft (0.76 m) and a span of 8 ft (2.44 m), which was fixed by two endplates and placed along the longitudinal centre line of the wind tunnel, and the rain manifold was placed 25 ft (7.62 m) in front of the leading edge of the aerofoil. In the simulations, the computational domain and boundary condition were established based on the characteristic size of the wind tunnel and the position arrangement of the model and equipment, as shown in Fig. 11. The face in front of the aerofoil was set as a velocity-inlet. The dynamic pressure of the incoming flow was consistent with that in the wind tunnel test, and the initial density of the rain phase was set to 0 $g/m^3$ in the no-rain condition and 25 $g/m^3$ in the rain condition. The face opposite to the velocity-inlet was set as a zero-pressure-outlet. The other faces were set as stationary walls in the computational domain.

The drag coefficient results of the aerofoil in the wind tunnel test and the numerical simulation under no-rain conditions are shown in Fig. 12(a), while the comparison of the results

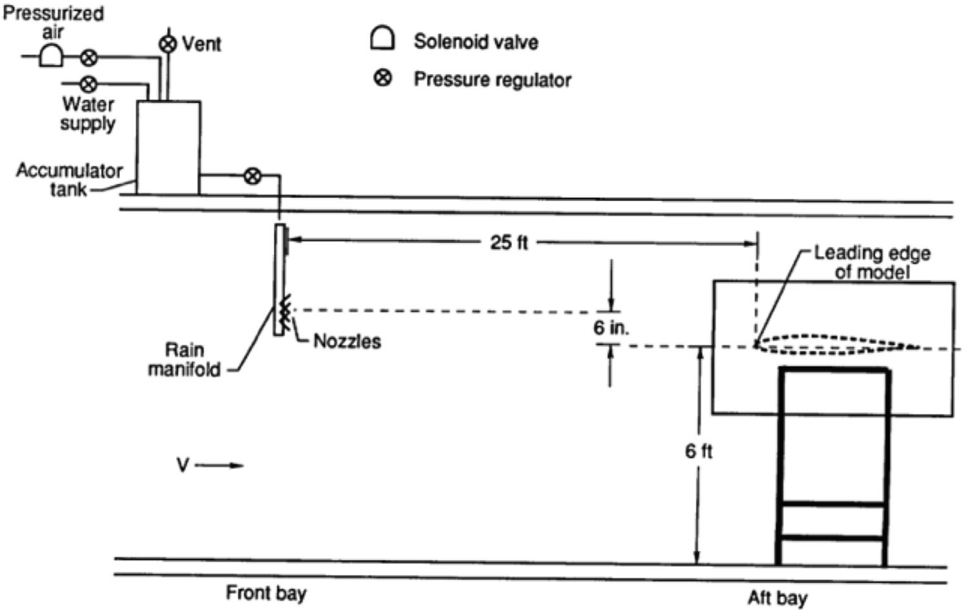

**Fig. 9** Wind tunnel test schematic diagram and parameters (adapted from Bezos et al. [53]).

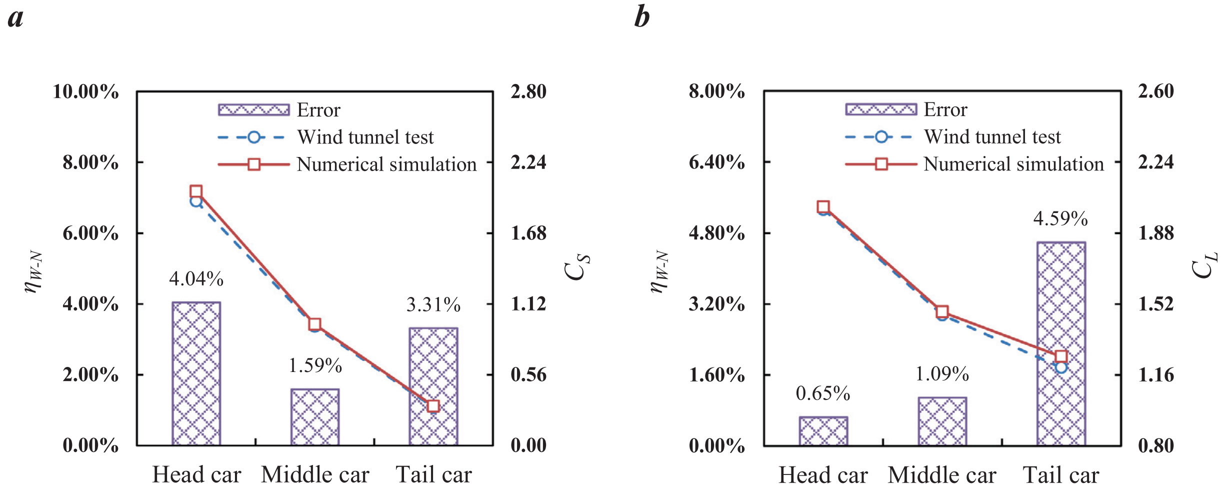

**Fig. 10** Result comparisons between wind tunnel test and numerical simulation: (a) $C_S$ and (b) $C_L$.

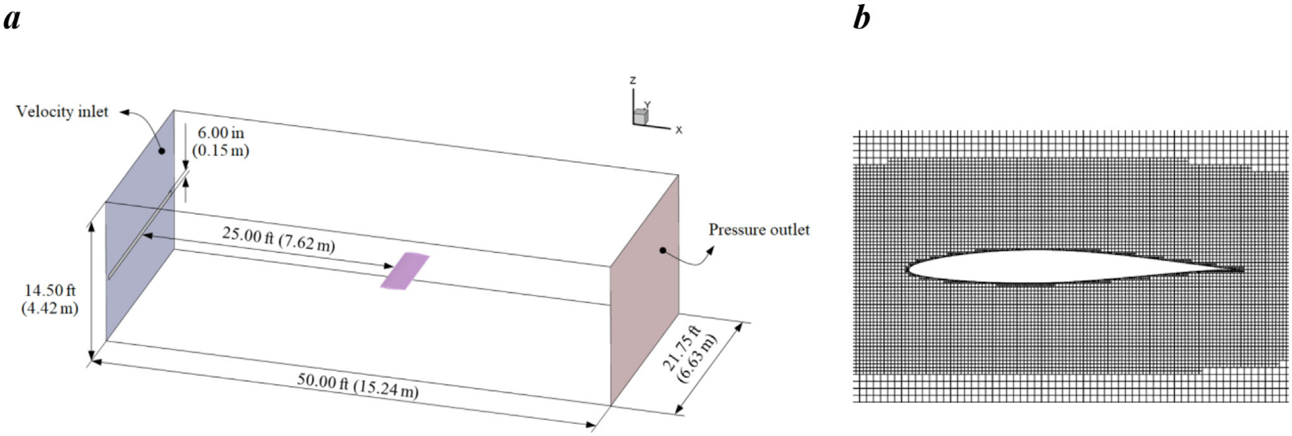

**Fig. 11** Computational domain and grid.

under rain conditions is shown in Fig. 12(b). The drag coefficient of the aerofoil showed an increasing tendency as the attack angle increased under the different conditions. The geometric model of the numerical simulation did not consider the holder and end plates of the aerofoil, and the rain manifold placed in the wind tunnel affected the incoming flow in the experiment, which led to different results between the numerical simulation and the wind tunnel experiment at high attack angles. However, the numerical simulation results were in good consistency with the wind tunnel experiment at lower attack angles, and the overall tendency was similar both in

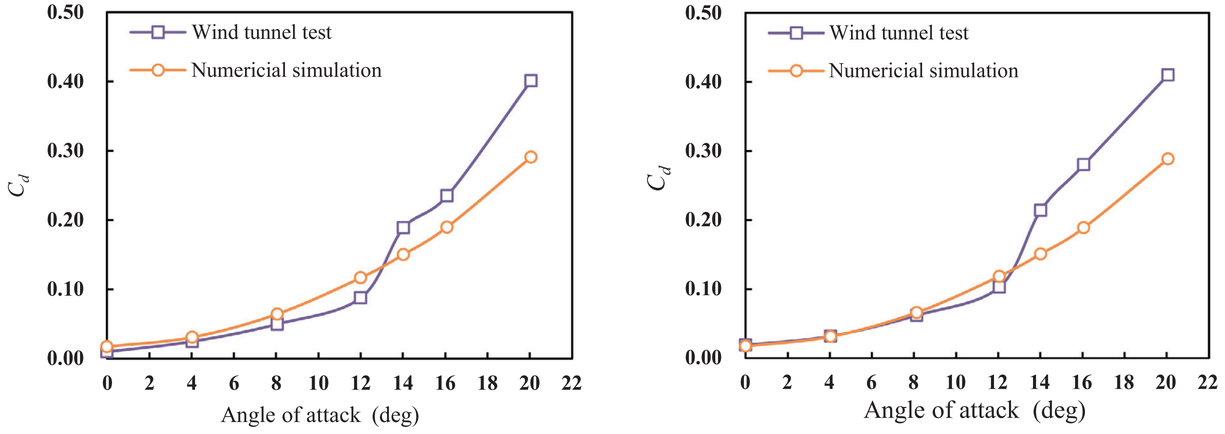

**Fig. 12** Result comparisons between wind tunnel test and numerical simulation: (a) no-rain conditions and (b) rain conditions.

no-rain and rain conditions, proving the numerical method was accurate and appropriate for this study.

## 4. Results analysis and discussions

### 4.1. Impact of crosswind speed

### 4.1.1. Raindrop density around train

As the train and bridge were exposed to the wind and rain environment, the raindrops density around the train and bridge may reveal the airflow fluctuations situation. Therefore, to compare the variation of the raindrop density distribution around the train and bridge, the slices in the middle position of the head car, middle car, and tail car were chosen for analysis, as shown in Fig. 13.

To ensure that the comparison was effective, conditions with varying crosswind speeds under a rainfall of 60 mm/h and the train's running speed of 200 km/h were chosen for analysis. The raindrop density around each slice of the train and bridge is shown in Fig. 14. Raindrops in the air impacted the windward side surface (WWS-S) of the train and bridge under the action of a crosswind, as shown in Fig. 14. With the rise of the crosswind speed, the speed of the raindrops driven by the crosswind also increased, resulting in more raindrops covering the WWS-S of the train and bridge and demonstrating an increasing tendency of the raindrop density. Furthermore, under the action of gravity, some of the raindrops attached to the WWS-S of the train and bridge flowed down to the bridge floor and ground. Due to the rising trend of the airflow speed between the windward side and top of the train, some raindrops driven by the airflow around the

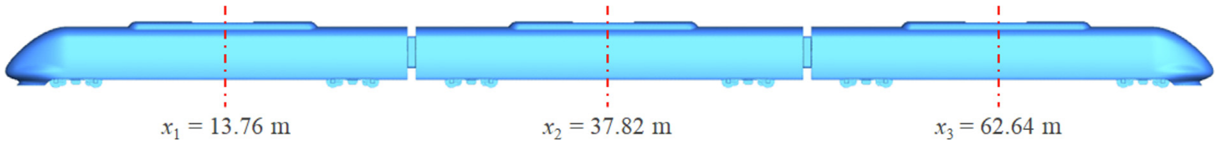

**Fig. 13** Definition of the locations of slices on the train.

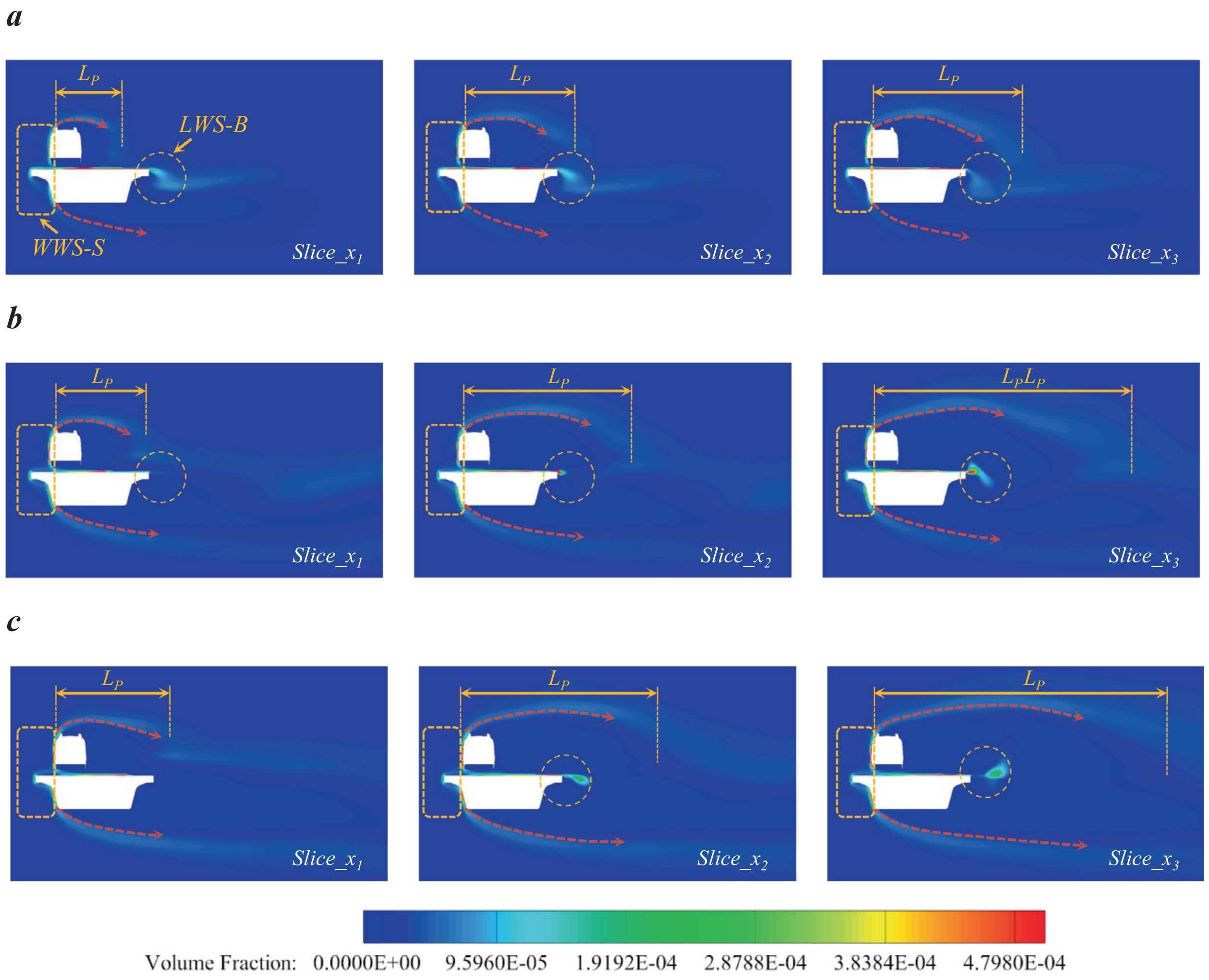

**Fig. 14** Raindrop density distributions under different wind speeds: (a) 10 m/s, (b) 20 m/s, and (c) 30 m/s.

train exhibited a parabolic projectile feature, as shown by the red arrows in Fig. 14. The projectile distance, i.e., $L_p$ in Fig. 14, showed an increasing tendency with the increase in the crosswind speed, and the $L_p$ values around the middle car and tail car were greater than that of the head car, which was likely because the airflow around the leeward side of the train intensified along the longitudinal direction of the train and bridge. This phenomenon was also demonstrated in the area between the windward side and the bottom of the bridge. Meanwhile, the projectile distances under the bridge were more significant than at the top of the train at lower crosswind speeds. However, for the higher crosswind speed, discrepancies in the projectile distance between the top of the train and the bottom of the bridge were not evident. Furthermore, the airflow action caused raindrops that accumulated on the bridge floor to be thrown along the leeward side of the bridge (LWS-B), as shown in the regions of the LWS-B in Fig. 14. The projectile feature was more significant with the increase in the crosswind speed and rise of the longitudinal direction of the train and bridge. This was probably because vortices formed and stretched on the leeward side of the train as well as on the bottom and leeward side of the bridge, driving raindrops to be thrown to the leeward side. Thus, the raindrop density on the leeward side of the train and bridge was lower, and this area demonstrated an increasing tendency as the crosswind speed increased.

### 4.1.2. Pressure on train surface

Due to the significant driving effect of the coupled wind formed by the crosswinds and the slipstream induced by the train on the raindrops, the head car was impacted by raindrops more violently than the other carriages of the train. Two lines on cross-sectional planes in the vertical section, i.e., $X$-directions, and horizontal longitudinal section, i.e., $Z$-directions, were obtained to estimate the pressure coefficient distribution of the head car, as shown in Fig. 15(a). The two lines were all divided into several sections, as shown in Fig. 15(a), (b), and (c). To ensure the effectiveness of the comparison results, the pressure coefficient $C_p$ is defined as follows:

$$C_P = (P_i - P_0)/(0.5\rho V_{couple}^2) \tag{21}$$

where $P_i$ is the pressure of a certain point in the space of the computational domain, and $P_0$ is the reference pressure, which was 0 Pa.

Under a rainfall of 60 mm/h and the train operating speed of 200 km/h, the pressure coefficient distributions around different lines are shown in Fig. 16. As shown in Fig. 16(a), under the crosswind speed of 10 m/s, the pressure coefficient of the train in the rain and no-rain conditions demonstrated similar variation trends, which was likely because the impact of the crosswind played a dominant role in the wind and rain environment. On the cross section of the head car, the windward side surface of the train (section A-B) was significantly affected by the crosswind, and the surface pressure coefficient was relatively high. Meanwhile, the crosswind drove the raindrops to impact the windward side surface of the train most violently, resulting in the pressure coefficient of section A-B under rain conditions being higher than that under no-rain conditions. As the curvature changed significantly at the transition arc from the sidewall to the roof of the train, the airflow separation led to significant pressure fluctuations in section B-C. However, in sections B-C and C-D, there were no significant variations in the pressure coefficient between the rain and no-rain conditions owing to raindrops being driven by crosswinds and thrown to the leeward side of the train. For the leeward side and bottom of the train (sections C-D and D-A), the pressure coefficient variation trends were smaller and gentle than those of the windward side and roof of the train, respectively. Nevertheless, the crosswind action was weaker than that of the slipstream induced by the train at lower speeds, which caused a stronger pressure pulsation to be generated under the streamlined head of the head car and enhanced the impact of raindrop particles on its bottom. Thus, a significant discrep-

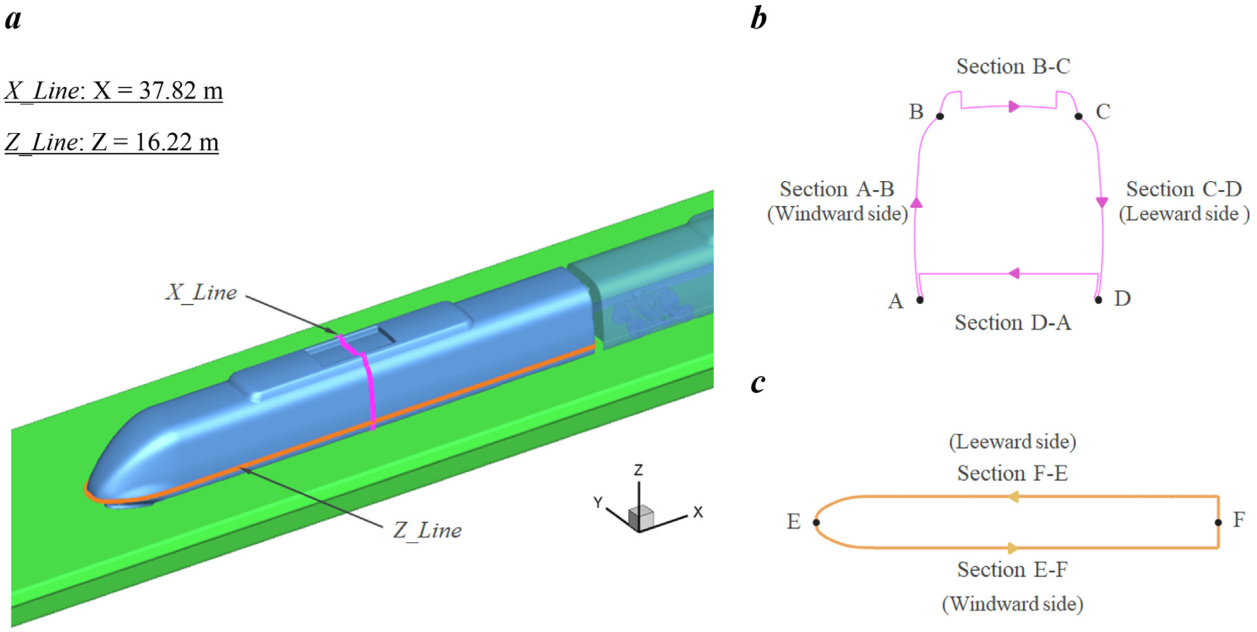

**Fig. 15** Definition of the lines on the train surface: (a) location, (b) division of *X_Line*, and (c) division of *Z_Line*.

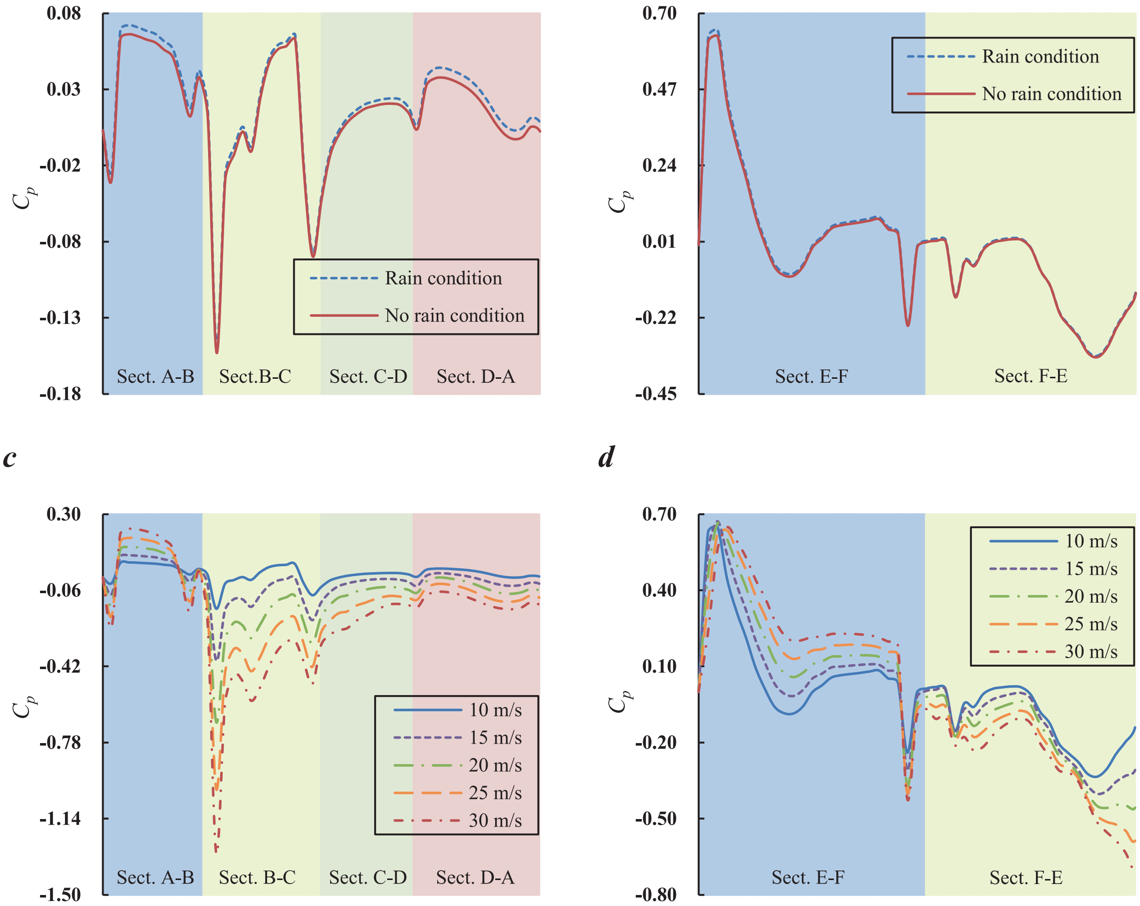

**Fig. 16** Pressure distributions around lines: (a) *X_Line* under rain and no-rain conditions, (b) *Z_Line* under rain and no-rain conditions, (c) comparison of different wind speeds of *X_Line*, and (d) comparison of different wind speeds of *Z_Line*.

ancy between the rain and no-rain conditions was evident at section D-A.

Furthermore, under the crosswind speed of 10 m/s, the pressure coefficient distribution of the head car in the horizontal direction is shown in Fig. 16(b). Due to the combined action of the crosswind and slipstream induced by the train, the windward side surface of the train (section E-F), especially the side of the train nose near the windward side, was impacted by raindrops relatively significantly. Therefore, the pressure coefficient exhibited a significant increasing trend under rain conditions. With the change of the longitudinal distance, the surface pressure coefficient showed a gentle declining trend, with the expected fluctuation characteristics in the windshield position owing to the airflow separation. The surface pressure coefficient on the train's leeward side (section F-E) was lower than that of the windward side, and the discrepancy between the rain and no-rain conditions was not noticeable on the leeward side.

As shown in Fig. 16(c) and (d), with the crosswind rising, the surface pressure coefficient of the train exhibited a similar variation tendency in the sections of *X_line* and *Z_line*, and it also showed a growing trend. Because the yaw angle increased with the increase in the crosswind speed under the same operating speed of the train, the amplitude of the pressure coefficient on the horizontal section tended to shift in the longitudinal direction. Thus, the pressure fluctuations on both sides of the train nose were more significant, as shown in Fig. 16(d).

### 4.1.3. Aerodynamic load coefficient

Under the rain and no-rain conditions, as the train ran at 200 km/h, the variations of the aerodynamic load coefficients of the whole train with the crosswind speed are shown in Fig. 17. At the same crosswind and operating speed of the train, the discrepancy percentages of the aerodynamic loads under rain conditions compared with no-rain conditions are also shown in the bar graphs in Fig. 17. Under different crosswind speed conditions, the $C_S$ and $C_M$ values of the whole train increased with the increase in the crosswind speed, as shown in Fig. 17(a) and (c). Due to raindrops driven by crosswind and impacting the train's surface, the $C_S$ of the train under rain conditions showed an increasing trend compared with that under no-rain conditions. Furthermore, the discrepancy of $C_S$ of the whole train under the rain and no-rain conditions showed a decreasing trend with the increase in the crosswind speed, which meant that the rainfall had a more noticeable effect on the $C_S$ under low crosswind speeds. The same variation tendency was evident for $C_M$, because the overturning moment of the whole train was produced by the combined action of the side and lift forces of the whole train, and the side force had a more significant effect.

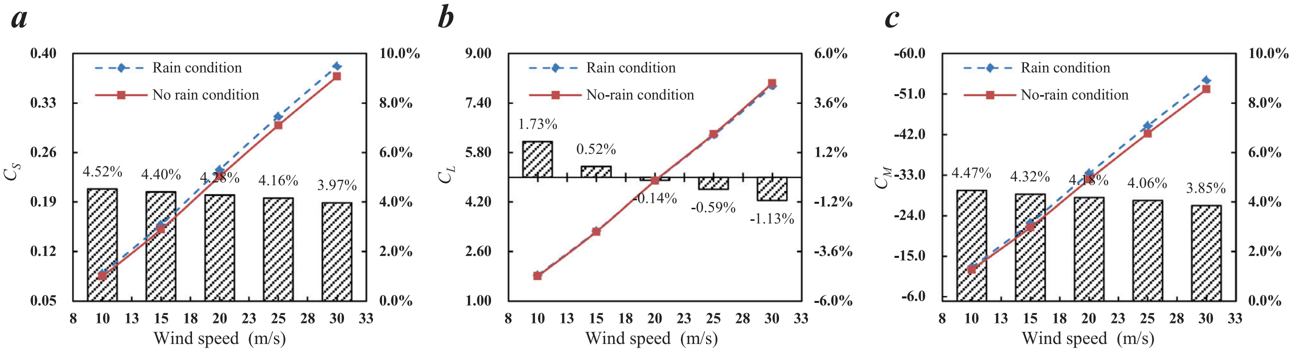

**Fig. 17** Comparison of aerodynamic force coefficients: (a) $C_S$, (b) $C_L$, and (c) $C_M$.

With the increase in the crosswind speed, a rising trend of $C_L$ of the whole train was evident under rain and no-rain conditions, as shown in Fig. 17(b). Nevertheless, the crosswind action was weaker than that of the slipstream induced by the train at lower crosswind speeds, which caused a stronger pressure pulsation to be generated under the bottom of the train and enhanced the impact of the raindrop particles on its bottom. Thus, the $C_L$ of the train under rain conditions tended to increase compared with that under no-rain conditions. However, with the gradual increase in the crosswind speed, more raindrops were driven by the crosswind and brought into the area around the train, and thus, the effect of raindrops on the vertical direction of the train was enhanced owing to the combined action of coupled airflow and gravity. Therefore, the $C_L$ of the whole train under rain conditions showed a downward trend compared to that under the no-rain conditions at higher crosswind wind speeds. Under the same rainfall, the aerodynamic loads of the whole train varied as the crosswind speed increased at different operating speeds, as shown in Fig. 18. $C_S$, $C_L$, and $C_M$ of the whole train demonstrated similar trends of increasing with the increase in the crosswind speed and decreasing with the decrease in the train speed.

As the analysis above, the effect of slipstream induced by the train combined with the crosswind on the aerodynamic loads of the train played a predominant role, while the role of rainfall on the tendency was less influential. Thus, at various operating speeds of the train, the variation of the aerodynamic loads impacted by the increased crosswind speeds in different rainfall was similar. To describe this, the average increase rate, which was the mean value of the aerodynamic loads at the same crosswind speed and different rainfall and operating speed of the train, was introduced to show the discrepancy of $C_S$, $C_L$ and $C_M$ of the whole train varying with the crosswind speed. Compared to the scenario of 10 m/s, the average increase rate of $C_S$ has 79.87 %, 166.77 %, 258.82 %, and 354.37 % increase with the increase of the crosswind speed in 15, 20, 25 and 30 m/s. Furthermore, based on this quantity, a minor decrease was noted when the train's operating speed rose, while a slight increase was observed as the train's operating speed declined. In addition, this regularity was also found in the average increase rate of $C_L$ and $C_M$ across the whole train. Compared to the 10 m/s crosswind scenario, the average variation of $C_L$ of the whole train increased by 79.52 %, 167.71 %, 256.19 % and 369.60 %, while $C_M$ of the whole train increased by 79.93 %, 166.91 %, 259.19 % and 355.07 %, with the increasing of crosswind speed.

### 4.2. Impact of different rainfall

#### 4.2.1. Raindrop density around train

To ensure that the comparison was reliable, under the crosswind speed of 20 m/s and the train operating speed of 200 km/h, the raindrop densities around each slice of the train and bridge are shown in Fig. 19. With the increase in the rainfall in the range of 20–100 mm/h, the raindrop density around the train and bridge demonstrated a growing trend. Due to the increased raindrop density with the rainfall increasing, raindrops driven by the crosswind were broken and then splashed and covered the surface of the train and bridge, resulting in the

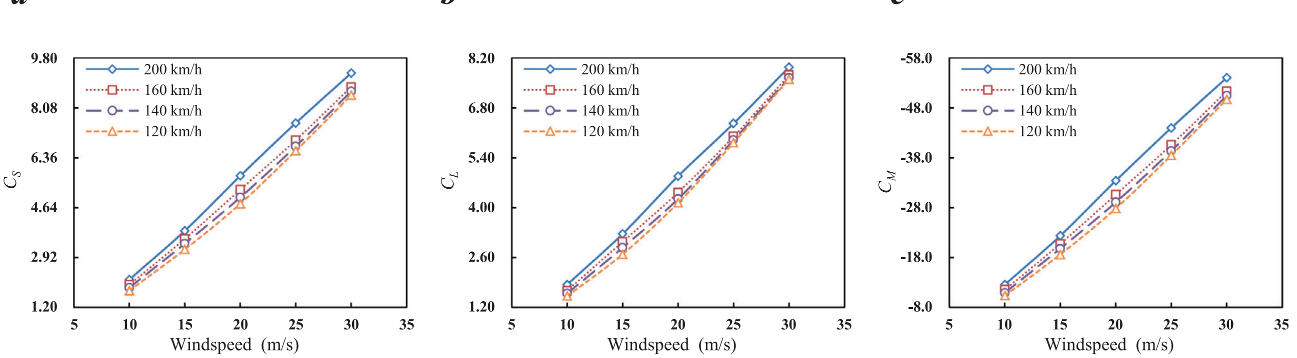

**Fig. 18** Comparison of aerodynamic force coefficients: (a) $C_S$, (b) $C_L$, and (c) $C_M$.

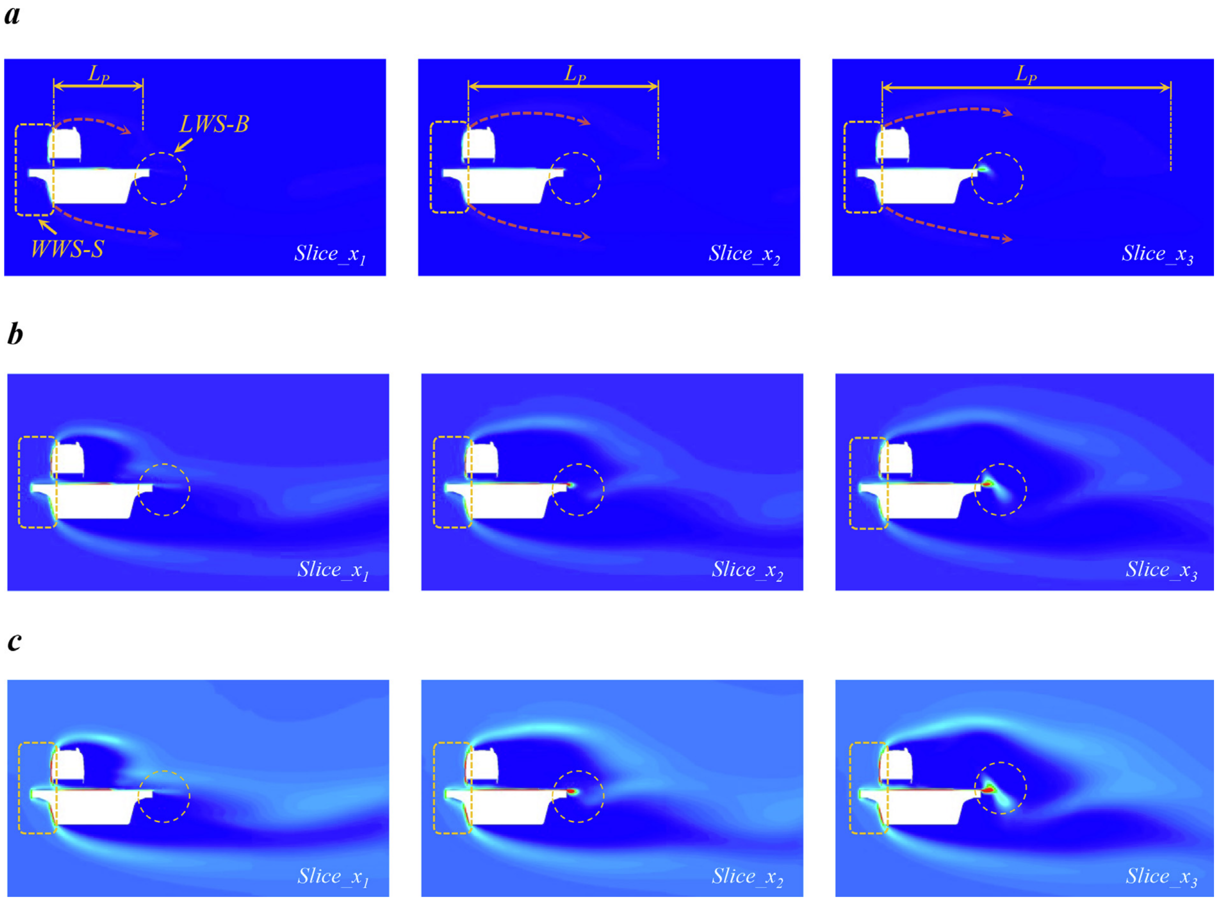

**Fig. 19** Raindrop density distribution under different rainfall amounts: (a) 20 mm/h, (b) 60 mm/h, and (c) 100 mm/h.

volume fraction of raindrops on the WWS-S of the train and bridge increasing. Furthermore, raindrops driven by the airflow intensified along the longitudinal direction of the train and bridge, so the $L_p$ of the tail car from the roof near the windward side to the leeward side was the longest, while that of the head car was the shortest, as shown in Fig. 19.

However, with increasing rainfall, differences of $L_p$ at the same longitudinal slices were not evident, which was likely because the impact of the crosswind on the flow field around the structures was predominant while the effects of raindrops were weaker in the wind and rain environment. Thus, affected by the airflow separation caused by the bridge and vortex development, some of the raindrops were affected by turbulent vortices, and the $L_p$ of the raindrops also showed a trend of increasing along the longitudinal direction of the train. In addition, the number of raindrops accumulated on the bridge floor showed a rising trend with increasing rainfall.

### 4.2.2. Pressure on train surface

Under the crosswind speed of 20 m/s and the train's operating speed of 200 km/h, the pressure coefficient distributions in the vertical and horizontal longitudinal sections of the head car are shown in Fig. 20. The rainfall amounts of 20, 40, 60, 80, and 100 mm/h, representing light, moderate, heavy, torrential, and heavy rain, respectively, followed similar trends to those of the pressure coefficient. Furthermore, as shown in Fig. 20(b), the amplitude shift of the pressure coefficient in the longitudinal direction on the horizontal section was not as significant as that of the crosswind speed variation. Thus, the increase in the rainfall had little effect on the airflow around the head of the train, and the crosswind effect was more significant than the impact of raindrops on the surface pressure coefficient of the train under the wind and rain environment.

To investigate the surface pressure coefficient of the train under different rainfall amounts, the peak values of the surface pressure coefficients in each section were utilised for comparative analysis, and the variation rate of the peak value of the pressure coefficient is defined as follows:

$$\eta_p = \frac{(C_{pr} - C_{p0})}{C_{p0}} \times 100\% \tag{22}$$

where $C_{p0}$ is peak value of the train surface pressure coefficient under no-rain conditions, and $C_{pr}$ is the peak value of the train surface pressure coefficient for different rainfall amounts.

The peak values and variation rates of the surface pressure coefficient of the head car for different rainfall amounts are shown in Tables 2 and 3. With the increase in the rainfall amount, the effect of the impact of raindrops on the windward surface of the train was enhanced, and the peak value of the surface pressure coefficient on the windward side (sections A-B and E-F) showed a significant increasing trend. However, the increased rainfall also resulted in an increased number of raindrops filling the air, and the probability of collision and fusion under the action of coupled airflow showed a significant

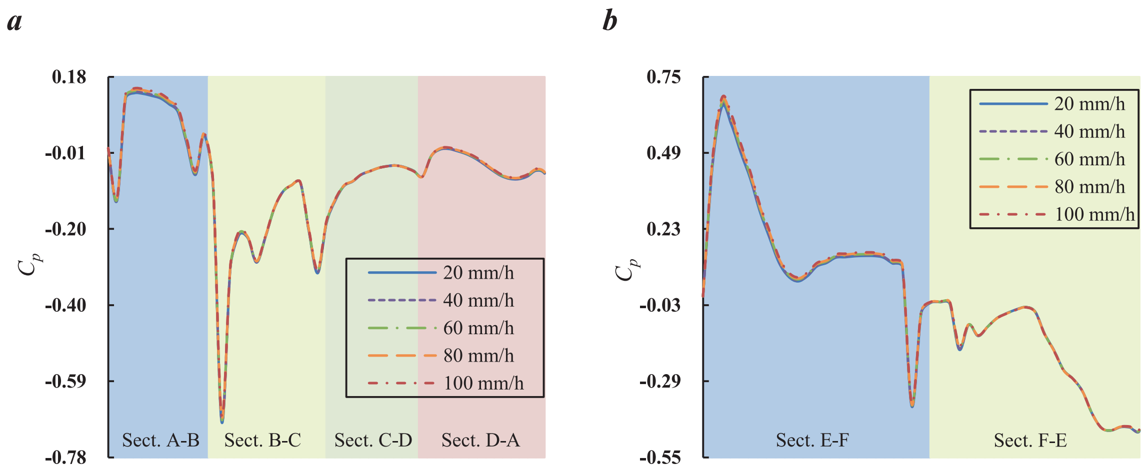

**Fig. 20** Pressure distributions around lines: comparison for different rainfall amounts along (a) *X_Line* and (b) *Z_Line*.

**Table 2** Comparison of the peak values of each section of *X_Line*.

| Section | 20 mm/h | | 40 mm/h | | 60 mm/h | | 80 mm/h | | 100 mm/h | |
|---|---|---|---|---|---|---|---|---|---|---|
| | $C_p$ | $\eta_p$ | $C_p$ | $\eta_p$ | $C_p$ | $\eta_p$ | $C_p$ | $\eta_p$ | $C_p$ | $\eta_p$ |
| A-B | 0.139 | 1.64 % | 0.142 | 3.63 % | 0.144 | 5.76 % | 0.148 | 8.06 % | 0.151 | 10.43 % |
| B-C | 0.691 | −0.40 % | 0.687 | −0.89 % | 0.683 | −1.43 % | 0.679 | −2.02 % | 0.675 | −2.64 % |
| C-D | 0.133 | −0.61 % | 0.132 | −1.23 % | 0.131 | −1.88 % | 0.130 | −2.60 % | 0.129 | −3.28 % |
| D-A | 0.109 | −0.86 % | 0.108 | −1.85 % | 0.107 | −2.95 % | 0.106 | −4.05 % | 0.104 | −5.21 % |

**Table 3** Comparison of the peak values of each section of *Z_Line*.

| Section | 20 mm/h | | 40 mm/h | | 60 mm/h | | 80 mm/h | | 100 mm/h | |
|---|---|---|---|---|---|---|---|---|---|---|
| | $C_p$ | $\eta_p$ | $C_p$ | $\eta_p$ | $C_p$ | $\eta_p$ | $C_p$ | $\eta_p$ | $C_p$ | $\eta_p$ |
| E-F | 0.648 | 0.81 % | 0.655 | 1.88 % | 0.662 | 3.03 % | 0.670 | 4.27 % | 0.679 | 5.55 % |
| F-E | 0.459 | −0.14 % | 0.458 | −0.37 % | 0.458 | −0.43 % | 0.458 | −0.46 % | 0.457 | −0.51 % |

upward trend. For this reason, the number of raindrops driven by airflow decreased owing to the gravitational effect, and their impact on the train surface was weakened. Thus, the peak values of the pressure coefficients on the roof, leeward side, and bottom sections (i.e., sections B-C, C-D, and D-A) of *X_line* and *Z_line* along the train surface all showed a downward trend with the increase in the rainfall. The value at the bottom (section D-A) was the largest, followed by that on the leeward side (C-D), and the value on the roof (section B-C) was the smallest.

### *4.2.3. Aerodynamic load coefficient*

When the train ran at 200 km/h, the aerodynamic load coefficient of the whole train varied with the rainfall, which is shown in Fig. 21. The bar graph represents the differences of the aerodynamic loads compared to those under the no-rain condition with the same crosswind speed and operating speed of the train. With the increase in the rainfall, the number of raindrops around the train showed an increasing trend. Therefore, the impact on the train's side surface was enhanced when the raindrops driven by the crosswind, and the $C_S$ of the whole train increased linearly with the increase in the rainfall amount, as shown in Fig. 21(a). The $C_L$ of the whole train varied with the rainfall amount, as shown in Fig. 21(b). Due to more raindrops being brought to the upper side of the train by the coupled airflow with the increasing rainfall amount, the impact on the vertical direction of the train tended to increase, and it also inhibited the driving force of the airflow under the train bottom to a certain extent. As a result, the $C_L$ of the whole train exhibited a decreasing trend with the increase in the rainfall, but the decreasing amplitude was relatively small because most raindrops were driven by the airflow and thrown to the leeward side of the train and bridge. In addition, since the variation of the rainfall had a relatively weak effect on the lift coefficient of the train, the trend of $C_M$ was basically consistent with that of $C_S$ as the rainfall amount increased, as shown in Fig. 21.

Under the same crosswind speed, the aerodynamic load of the whole train varied as the rainfall increased at different operating speeds, as shown in Fig. 22. Under the different operating speeds, $C_S$ and $C_M$ of the whole train showed the same trend of increasing with the increase in the rainfall amount, as shown in Fig. 22(a) and (c), while $C_L$ dropped slightly with the increase in the rainfall amount, as shown in

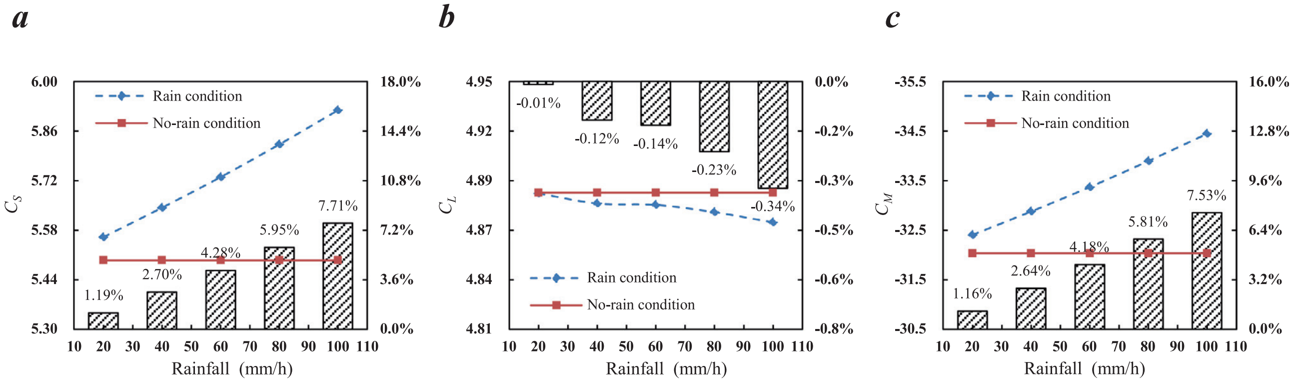

**Fig. 21** Comparison of aerodynamic force coefficients: (a) $C_S$, (b) $C_L$, and (c) $C_M$.

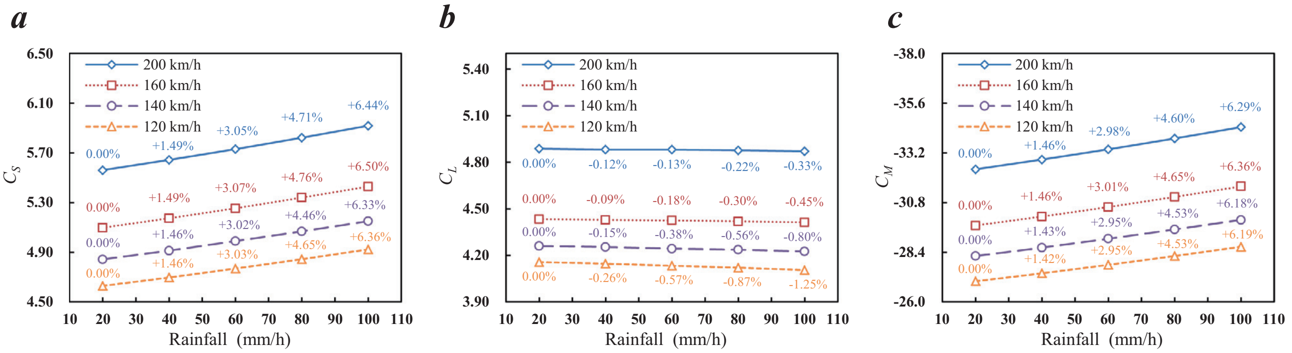

**Fig. 22** Comparison of aerodynamic force coefficients: (a) $C_S$, (b) $C_L$, and (c) $C_M$.

Fig. 22(b). In addition, compared to the rainfall amount of 20 mm/h, the percentage differences of $C_S$, $C_L$, and $C_M$ of the whole train under different rainfall amounts under the operating speeds of 200, 160, 140, and 120 km/h are also shown in Fig. 22. Under the same operating speed of the train, the rates of the aerodynamic load coefficient increase with increasing rainfall amount were similar, which was likely because of the additional influence of the rainfall in the wind and rain environment. Furthermore, with a decrease in the running speed of the train, $C_S$, $C_L$ and $C_M$ both showed a decreasing tendency at the same rainfall amount and crosswind speed.

The variation of aerodynamic load coefficients, which was affected by rainfall at different crosswind speeds, was similar, while this tendency was also similar during the reduction of the operating speed of the train. Thus, the average change rate, which was the mean value of the aerodynamic loads in the same rainfall and different crosswind speed and operating speed of the train, was introduced to illustrate the discrepancy of $C_S$, $C_L$ and $C_M$ with the varying rainfall. Compared with the scenario of 20 mm/h rainfall, an average change rate of $C_S$ was shown in an increase of 1.48 %, 3.04 %, 4.69 %, and 6.41 % in a rainfall of 40, 60, 80 and 100 mm/h. Furthermore, based on this quantity, a minor increase was noted when the train's operating speed rose, while a slight reduction was observed as the train's operating speed declined. In addition, $C_M$ of the whole train also showed a similar variation tendency and quantity of the average change rate with that of $C_S$ compared to the scenario of 20 mm/h rainfall, which increased by 1.44 %, 2.97 %, 4.58 % and 6.25 % in a rainfall range of 40–100 mm/h. In terms of $C_L$ of the whole train, a slight decrease was observed in the average change rate. The average variation rate of $C_L$ decreased by 0.15 %, 0.32 %, 0.49 % and 0.71 %, compared to the 20 mm/h rainfall scenario.

## 5. Conclusions

Based on the standard $k$-ε turbulent model and Euler multiphase model, the influences of the crosswind speed and rainfall on the aerodynamic performances of intercity trains running on bridges were investigated and validated against wind tunnel experimental results in this paper. The raindrop density distributions as well as surface pressure and aerodynamic forces of the train were discussed. The significant conclusions can be summarised as follows:

(1) With the increase in the crosswind speed and rainfall amount, the raindrop density around the surface of the train and bridge showed an increasing trend. Some raindrops presented a parabolic projectile feature, and their projectile distance increased with the increase in the crosswind speed. However, the projectile feature and the projectile distance of the raindrops were relatively less affected by the rainfall.

(2) Under the wind and rain environment, the effect of crosswinds played a dominant role, while raindrops provided additional effects. Thus, the distributions of the

surface pressure coefficient were similar in the rain and no-rain conditions and showed increasing trends with the increase in the crosswind speed and rainfall amount.

(3) With the increase of crosswind speed in rain conditions, both aerodynamic force and rolling moment showed increasing trends. An increase of 79.87 %–354.37 % was demonstrated in the average increase rate of $C_S$ of the whole train as the crosswind speed increased in a range of 15–30 m/s with the rain condition, compared to the crosswind speed conditions of 10 m/s. Also, the average increase rate of $C_L$ and $C_M$ of the whole train showed an increasing tendency of 79.52 %–369.60 % and 79.93 %–355.07 %, respectively.

(4) In wind and rain conditions, owing to the effect of crosswind driven raindrops, the average change rate of $C_S$ and $C_M$ of the whole train increased by 1.48 %–6.41 % and 1.44 %–6.25 %, respectively, in an increasing range of the rainfall in 20–100 mm/h with crosswind condition, compared to the 20 mm/h rainfall scenario. However, in terms of $C_L$ of the whole train, a slight decrease was observed in the average change rate, which decreased by 0.15–0.71 % with the rainfall increasing.

In the current work, the variation of the surface pressure and aerodynamic load coefficient of the train running on the bridge under different crosswind speeds and rainfall was compared and investigated in detail, which could provide a theoretical reference for those who are concerned about the structures' design of intercity trains and bridges and to improve the operation safety of the train. Due to the complexity of the multiphase flow in wind and rain environment, the influence of different turbulent models and operating schemes of the train as well as more factors could be further investigated to reveal the coupled effect on the aerodynamic performance of the train running on the bridge in the further works.

## Declaration of Competing Interest

The authors declare that they have no known competing financial interests or personal relationships that could have appeared to influence the work reported in this paper.

## Acknowledgement

This work was supported by the National Natural Science Foundation of China (Grant No. 52002290, Grant No. 52202426), Natural Science Foundation of Guangdong Province (Grant No. 2022A1515010011), Fundamental Science and Technology Projects of Jiangmen (Grant No. 2019JC01021, Grant No. 2021030102780006189), Hong Kong and Macau Joint Research and Development Fund of Wuyi University (Grant No. 2019WGALH17), the Open Project of Key Laboratory of Traffic Safety on Track of Ministry of Education (Grant No. 502401002), and The Hong Kong Polytechnic University's Postdoc Matching Fund Scheme (Grant No. 1-W16W).

## References

[1] M. Li, X. Zhou, Y. Wang, L. Jia, M. An, Modelling cascade dynamics of passenger flow congestion in urban rail transit network induced by train delay, Alexandria Eng. J. 61 (11) (2022) 8797–8807.

[2] X. Huo, T. Liu, Z. Chen, W. Li, H. Gao, S. Wang, Comparative analysis of the aerodynamic characteristics on double-unit trains formed by different types of high-speed train, J. Wind Eng. Ind. Aerodyn. 217 (2021) 104757.

[3] Z. Chen, T. Liu, X. Zhou, X. Su, Aerodynamic analysis of trains with different streamlined lengths of heads, 2016 IEEE International Conference on Intelligent Rail Transportation (ICIRT), IEEE, 2016.

[4] B. Ning, T. Tang, H. Dong, D. Wen, D. Liu, S. Gao, J. Wang, An introduction to parallel control and management for high-speed railway systems, IEEE Trans. Intell. Transp. Syst. 12 (4) (2011) 1473–1483.

[5] L. Yan, The linear motor powered transportation development and application in China, Proc. IEEE 97 (11) (2009) 1872–1880.

[6] G. Lombaert, G. Degrande, Ground-borne vibration due to static and dynamic axle loads of InterCity and high-speed trains, J. Sound Vib. 319 (3–5) (2009) 1036–1066.

[7] W. Sun, J. Jia, Research on optimizing the operating project about intercity passenger train, Proceedings. The 7th International IEEE Conference on Intelligent Transportation Systems (IEEE Cat. No. 04TH8749), IEEE, 2004.

[8] Y. Zou, Y. Zhang, H. Mao, Fault diagnosis on the bearing of traction motor in high-speed trains based on deep learning, Alexandria Eng. J. 60 (1) (2021) 1209–1219.

[9] B. Diedrichs, M. Sima, A. Orellano, H. Tengstrand, Crosswind stability of a high-speed train on a high embankment, Proc. Inst. Mech. Eng., Part F: J. Rail Rapid Transit 221 (2) (2007) 205–225.

[10] S. Giappino, D. Rocchi, P. Schito, G. Tomasini, Cross wind and rollover risk on lightweight railway vehicles, J. Wind Eng. Ind. Aerodyn. 153 (2016) 106–112.

[11] C. Baker, M. Sterling, The calculation of train stability in tornado winds, J. Wind Eng. Ind. Aerodyn. 176 (2018) 158–165.

[12] L. Zhang, M. Yang, X. Liang, Experimental study on the effect of wind angles on pressure distribution of train streamlined zone and train aerodynamic forces, J. Wind Eng. Ind. Aerodyn. 174 (2018) 330–343.

[13] Z. Guo, T. Liu, Z. Chen, Z. Liu, A. Monzer, J. Sheridan, Study of the flow around railway embankment of different heights with and without trains, J. Wind Eng. Ind. Aerodyn. 202 (2020) 104203.

[14] Z. Chen, Y. Ni, Y. Wang, S. Wang, T. Liu, Mitigating crosswind effect on high-speed trains by active blowing method: a comparative study, Eng. Appl. Comput. Fluid Mech. 16 (1) (2022) 1064–1081.

[15] Z. Chen, Y. Ni, Sudden flow induced by mountain ridges beside windbreaks in a railway and its mitigation measures, Transport. Safety Environ. 4 (1) (2022) tdac004.

[16] Z. Chen, T. Liu, Z. Jiang, Z. Guo, J. Zhang, Comparative analysis of the effect of different nose lengths on train aerodynamic performance under crosswind, J. Fluids Struct. 78 (2018) 69–85.

[17] T. Liu, Z. Chen, X. Zhou, J. Zhang, A CFD analysis of the aerodynamics of a high-speed train passing through a windbreak transition under crosswind, Eng. Appl. Comput. Fluid Mech. 12 (1) (2018) 137–151.

[18] Z. Chen, T. Liu, M. Li, M. Yu, Z. Lu, D. Liu, Dynamic response of railway vehicles under unsteady aerodynamic forces caused by local landforms, Wind Struct. 29 (3) (2019) 149–161.

[19] Z. Chen, T. Liu, W. Li, Z. Guo, Y. Xia, Aerodynamic performance and dynamic behaviors of a train passing through an elongated hillock region beside a windbreak under crosswinds and corresponding flow mitigation measures, J. Wind Eng. Ind. Aerodyn. 208 (2021) 104434.

[20] T. Liu, L. Wang, Z. Chen, H. Gao, W. Li, Z. Guo, Y. Xia, X. Huo, Y. Wang, Study on the pressure pipe length in train

aerodynamic tests and its applications in crosswinds, J. Wind Eng. Ind. Aerodyn. 220 (2022) 104880.

[21] J. Niu, Y. Zhang, R. Li, Z. Chen, H. Yao, Y. Wang, Aerodynamic simulation of effects of one-and two-side windbreak walls on a moving train running on a double track railway line subjected to strong crosswind, J. Wind Eng. Ind. Aerodyn. 221 (2022) 104912.

[22] N. Kumar, A. Mishra, A multi-objective and dictionary-based checking for efficient rescheduling trains, Alexandria Eng. J. 60 (3) (2021) 3233–3241.

[23] V. Chiu, H. Ge, T. Stathopoulos, Overhang effect on reducing wind-driven rain for a mid-rise building, Energy Proc. 78 (2015) 2506–2511.

[24] G. Arch, B. Hajra, M. Moravej, I. Zisis, P. Irwin, A. Chowdhury, W. Suaris, An experimental study to assess the effect of soffit louvered vents on wind loads and wind driven rain intrusion on low rise buildings, Sustainable Cities Soc. 34 (2017) 43–55.

[25] D. Xin, H. Li, L. Wang, J. Ou, Experimental study of rain effects on vortex shedding of long span bridge girders, Adv. Struct. Eng. 15 (10) (2012) 1793–1799.

[26] X. Shao, J. Wan, D. Chen, H. Xiong, Aerodynamic modeling and stability analysis of a high-speed train under strong rain and crosswind conditions, J. Zhejiang Univ.-Sci. A 12 (12) (2011) 964–970.

[27] Y. Cao, Z. Wu, Z. Xu, Effects of rainfall on aircraft aerodynamics, Prog. Aerosp. Sci. 71 (2014) 85–127.

[28] M. Ismail, C. Yihua, Z. Wu, M.A. Sohail, Numerical study of aerodynamic efficiency of a wing in simulated rain environment, J. Aircraft 51 (6) (2014) 2015–2023.

[29] Z. Wu, Drop "impact" on an airfoil surface, Adv. Colloid Interface Sci. 256 (2018) 23–47.

[30] Y. Yue, Q. Zeng, Z. Li, F. Lu, Numerical simulating effects of rain-loaded wind on the aerodynamic characterstics and running stability of high-speed trains, J. Desert Res. 36 (4) (2016) 943–950.

[31] J. Jing, G. Gao, Simulation of the action effect of wind-driven rain on high-speed train, J. Railway Sci. Eng. 10 (3) (2013) 99–102, in Chinese.

[32] L. Du, S. Ni, Influence of aerodynamic characteristics of a high-speed train under rain and lower atmospheric boundary layer crosswind conditions, J. Dalian Jiaotong Univ. 37 (5) (2016) 56–61, in Chinese.

[33] M. Yu, J. Liu, Z. Dai, Aerodynamic characteristics of a high-speed train exposed to heavy rain environment based on non-spherical raindrop, J. Wind Eng. Ind. Aerodyn. 211 (2021) 104532.

[34] ANSYS, ANSYS Fluent Theory Guide, ANSYS Inc, Canonsburg, PA, 2013.

[35] T. Liu, J. Zhang, Effect of landform on aerodynamic performance of high-speed trains in cutting under cross wind, J. Central South Univ. 20 (3) (2013) 830–836.

[36] Y. Li, H. Tian, M. Yang, Aerodynamic drag analysis of double-deck container vehicles with different structures, J. Central South Univ. Technol. 18 (4) (2011) 1311–1315.

[37] J. Zhang, G. Gao, T. Liu, Z. Li, Shape Optimization of a Kind of Earth Embankment Type Windbreak Wall along the Lanzhou-Xinjiang Railway, J. Appl. Fluid Mech. 10 (4) (2017) 1189–1200.

[38] A. Kubilay, D. Derome, B. Blocken, J. Carmeliet, CFD simulation and validation of wind-driven rain on a building facade with an Eulerian multiphase model, Build. Environ. 61 (2013) 69–81.

[39] K. Pettersson, S. Krajnovic, A. Kalagasidis, P. Johansson, Simulating wind-driven rain on building facades using Eulerian multiphase with rain phase turbulence model, Build. Environ. 106 (2016) 1–9.

[40] H. Fatahian, H. Salarian, M.E. Nimvari, J. Khaleghinia, Computational fluid dynamics simulation of aerodynamic performance and flow separation by single element and slatted airfoils under rainfall conditions, Appl. Math. Model. 83 (2020) 683–702.

[41] H. Fatahian, H. Salarian, M. Eshagh Nimvari, J. Khaleghinia, Numerical simulation of the effect of rain on aerodynamic performance and aeroacoustic mechanism of an airfoil via a two-phase flow approach, SN, Appl. Sci. 2 (5) (2020) 1–16.

[42] Y. Xi, J. Mao, G. Yang, Y. Fang, Research on influence of the type of cross wind field on the aerodynamic performance of a high-speed train, Proceedings of the 1st International Workshop on High-Speed and Intercity Railways, Springer, 2012.

[43] M. Zhang, Y. Lai, Z. Gao, W. Yu, Influence of boundary conditions on the cooling effect of crushed-rock embankment in permafrost regions of Qinghai-Tibetan Plateau, Cold Reg. Sci. Technol. 44 (3) (2006) 225–239.

[44] Y. Lai, M. Zhang, Z. Liu, W. Yu, Numerical analysis for cooling effect of open boundary ripped-rock embankment on Qinghai-Tibetan railway, Sci. China Series D 49 (7) (2006) 764–772.

[45] M. Liu, W. Ma, F. Niu, J. Luo, G. Yin, Thermal performance of a novel crushed-rock embankment structure for expressway in permafrost regions, Int. J. Heat Mass Transf. 127 (2018) 1178–1188.

[46] C. Lu, Q. Li, S. Huang, F. Chen, X. Fu, Large eddy simulation of wind effects on a long-span complex roof structure, J. Wind Eng. Ind. Aerodyn. 100 (1) (2012) 1–18.

[47] D.A. de Wolf, On the Laws-Parsons distribution of raindrop sizes, Radio Sci. 36 (4) (2001) 639–642.

[48] S. Huang, Q. Li, Numerical simulations of wind-driven rain on building envelopes based on Eulerian multiphase model, J. Wind Eng. Ind. Aerodyn. 98 (12) (2010) 843–857.

[49] Q. Jiang, J. Bian, Y. Li, Establishment of model prototype of raindrop dropping process, Plateau Meteorol. 39 (3) (2020) 609–619, in Chinese.

[50] H. Wang, W. Song, Y. Chen, Numerical simulation of wind-driven rain distribution on building facades under combination layout, J. Wind Eng. Ind. Aerodyn. 188 (2019) 375–383.

[51] EN14067-6, Railway applications Aerodynamics-Part 6: Requirements and test procedures for cross wind assessment, EN, 2010.

[52] J.D. Anderson, Fundamentals of aerodynamics, McGraw-Hill Education, 2010.

[53] G.M. Bezos, R.E. Dunham Jr, G.L. Gentry Jr, W.E. Melson Jr, Wind tunnel aerodynamic characteristics of a transport-type airfoil in a simulated heavy rain environment, NASA Langley Research Center, Hampton, VA, United States, 1992.

[54] Z. Chen, T. Liu, C. Yan, M. Yu, Z. Guo, T. Wang, Numerical simulation and comparison of the slipstreams of trains with different nose lengths under crosswind, J. Wind Eng. Ind. Aerodyn. 190 (2019) 256–272.